

Anomalous polarization reversal in strained thin films of CuInP_2S_6

Anna N. Morozovska ^{1,*} Eugene A. Eliseev ² Ayana Ghosh,³ Mykola E. Yeliseiev ⁴
Yulian M. Vysochanskii ^{5,†} and Sergei V. Kalinin^{6,‡}

¹*Institute of Physics, National Academy of Sciences of Ukraine, Nauky Avenue, Bldg. 46, 03028 Kyiv, Ukraine*

²*Institute for Problems of Materials Science, National Academy of Sciences of Ukraine, Krjijanovskogo Street, Bldg. 3, 03142 Kyiv, Ukraine*

³*Computational Sciences and Engineering Division, Oak Ridge National Laboratory, Oak Ridge, Tennessee 37831, USA*

⁴*Physics Faculty of Taras Shevchenko National University of Kyiv, Volodymyrska street 64, Kyiv 01601, Ukraine*

⁵*Institute of Solid-State Physics and Chemistry, Uzhhorod University, 88000 Uzhhorod, Ukraine*

⁶*Department of Materials Science and Engineering, University of Tennessee, Knoxville, Tennessee 37996, USA*



(Received 8 April 2023; revised 12 June 2023; accepted 10 August 2023; published 31 August 2023)

Strain-induced transitions of polarization reversal in thin films of a ferroelectric CuInP_2S_6 (CIPS) with ideally conductive electrodes are explored using the Landau-Ginzburg-Devonshire approach with an eighth-order free energy expansion in polarization powers. Due to multiple potential wells, the height and position of which are temperature and strain dependent, the energy profiles of CIPS can flatten in the vicinity of the nonzero polarization states. Thereby, we reveal an unusually strong effect of a mismatch strain on the out-of-plane polarization reversal, hysteresis loop shape, dielectric susceptibility, and piezoelectric response of CIPS films. By varying the sign of the mismatch strain and its magnitude in a fairly narrow range, quasistatic hysteresisless paraelectric curves can transform into double, triple, and other types of pinched and single hysteresis loops. The strain effect on the polarization reversal is opposite, i.e., anomalous, in comparison with many other ferroelectric films, for which the out-of-plane remanent polarization and coercive field increase strongly for tensile strains and decrease or vanish for compressive strains. For definite values of temperature and mismatch strain, the low-frequency hysteresis loops of polarization may exhibit negative slope in a relatively narrow range of external field amplitude and frequency. The low-frequency susceptibility hysteresis loops, which correspond to the negative slope of polarization loops, contain only positive values, which can be giant in the entire range of field changes. The corresponding piezoresponse also reaches giant values, being maximal near coercive fields.

DOI: [10.1103/PhysRevB.108.054107](https://doi.org/10.1103/PhysRevB.108.054107)

I. INTRODUCTION

The strain-tunable reversible spontaneous polarization of low-dimensional ferroic materials, including ferroelectrics, ferroelectrics, and antiferroelectrics (AFE) [1], is of great fundamental interest being directly defined by the interaction of lattice soft phonons with local atomic potential. Since the strain-tunable reversible polar properties are very attractive for advanced applications in nanoelectronics, sensorics, and three-dimensional (3D) multibit memory technologies, strain- and temperature-induced tunability of classical ferroelectric materials have been extensively explored.

Recently, ferroelectricity has been revealed in layered two-dimensional (2D) van der Waals (vdW) materials, such as $\text{CuInP}_2(\text{S,Se})_6$ monolayers, thin films, and nanoflakes [2,3]. The most important aspect of the physics of uniaxial ferroelectrics $\text{CuInP}_2(\text{S,Se})_6$ [4,5], compared with many other uniaxial ferroelectrics, is the existence of more than two potential wells [6], which leads to unique features of their polarization reversal, which are responsible for strain-tunable

multiple polar states. Due to multiple potential wells, whose height and position are temperature and strain dependent, the energy profiles of $\text{CuInP}_2(\text{S,Se})_6$ can flatten in the vicinity of the nonzero polarization states. That is, $\text{CuInP}_2(\text{S,Se})_6$ differs from classical ferroelectric materials with the first- or second-order ferroelectric-paraelectric (PE) phase transition, whose potential energy profiles can be shallow or flat near the transition point only, corresponding to zero spontaneous polarization. The flattened energy profiles in the vicinity of the nonzero polarization states, in turn, can give rise to enhanced polar and dielectric properties associated with polarization dynamics in the vicinity of the states.

The spontaneous polarization of crystalline CuInP_2S_6 (CIPS) is directed normally to its structural layers as a result of antiparallel shifts of the Cu^+ and In^{3+} cations from the middle of the layers [7,8]. The Cu^+ cations flip in their two-well local potential between Cu^{up} and Cu^{down} positions with a temperature increase and populate the positions with equal probability above the temperature of the transition from the polar ferroelectric to the nonpolar PE phase. The In^{3+} cations also contribute to the polar ordering of the CIPS crystal lattice, and the shift of the In^{3+} cations in their local potential is opposite to the deviation of Cu^+ cations from the middle of CIPS structural layers. Figure 1(a) shows the formation of so-called *intralayer* polarization states in CIPS

*anna.n.morozovska@gmail.com

†vysochanskii@gmail.com

‡sergei2@utk.edu

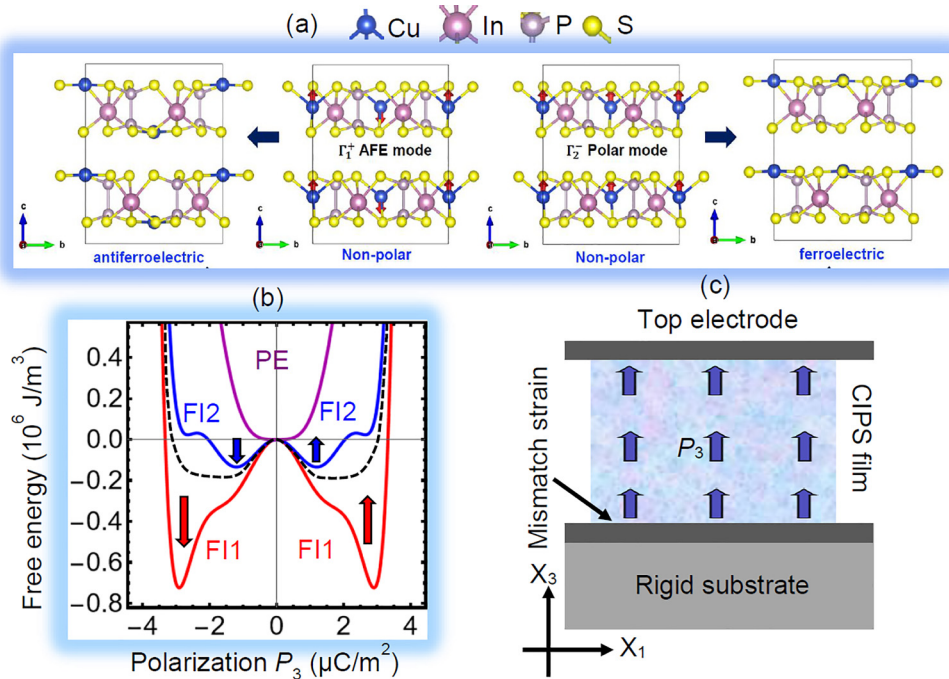


FIG. 1. (a) Structural models of CIPS with different polar phases. The nonpolar configuration is transformed to a ferroelectric one via the polar (ferroelectric) mode Γ_2^- . The Γ_1^+ mode, which is antiferroelectric (AFE) in nature, leads to the AFE phase. (b) Schematics of a potential relief in the paraelectric (PE) phase (the dark violet curve) and FI1 (the red curve) and FI2 (the blue curve) states. The FI1 and FI2 states merge in the bcritical endpoint (the black dashed curve), creating flattening of the free energy landscape around nonzero polarization. Up and down ferroelectric states with big (FI1) and small (FI2) amplitudes of the out-of-plane polarization are shown by the red and blue arrows. (c) A thin epitaxial CIPS film sandwiched between ideally conductive electrodes is clamped on a rigid substrate. Arrows show the direction of the spontaneous polarization.

with the spontaneous polarization $P_3 \sim 4 - 5 \mu\text{C/cm}^2$, which are studied in this paper. Note that Fig. 1(a) illustrates only polar and AFE modes involving the shift of Cu^+ cations. In a real CIPS structure, the mode of Cu^+ cations interplays with the oppositely polarized polar mode of In^{3+} cations, which leads to the ferroelectric ground state. The ferroelectric state with a high polarization $\sim 9 - 10 \mu\text{C/cm}^2$ can be induced only by a very high electric field that returns the In^{3+} cations to the middle of the structural layer or even into the direction of the Cu^+ cation shift.

In pseudospin formalism, the polar ordering of CIPS can be described by the Ising model with spins \vec{s} and \vec{S} and a mixed anisotropy of the local crystal field [9]. The spins \vec{s} with projections $+\frac{1}{2}$ and $-\frac{1}{2}$ can be associated with the local dipoles induced by Cu^+ cations and P_2S_6 anion complexes, and spins \vec{S} with projections $+1, 0, -1$ can be related to the local dipoles induced by In^{3+} cations and P_2S_6 anion complexes. In the Landau-Ginzburg-Devonshire (LGD) mean-field approximation [10,11], the presence of two types of cationic sublattices in ferroelectrics is described by polar and antipolar order parameters P and A , respectively. The polar and antipolar orders correspond to projections $S_z = \pm 1$ in the polar state and $S_z = 0$ in the nonpolar state.

Even though the antipolar order parameter A cannot be directly measured, a complete LGD thermodynamic potential for a ferroelectric with a first-order phase transition contains even (second, fourth, and sixth) powers of P and A , and the biquadratic coupling term between them $A^2 P^2$. As was shown

in Ref. [11], the biquadratic coupling term induces the term proportional to P^8 in the LGD thermodynamic potential for P . Using the LGD thermodynamic potential with eight powers of P , we predicted a temperature-stress phase diagram [11–13] containing the PE phase and two ferroelectric states FI2 and FI1, with smaller ($\sim 1 \mu\text{C/cm}^2$) and bigger ($\sim 4 \mu\text{C/cm}^2$) amplitudes of the spontaneous polarization [see Fig. 1(b)].

During the polarization reversal in CIPS, due to the antiparallel and antiphase displacement of the ferroactive Cu^+ and In^{3+} cations relative to the P_2S_6 sublattice [8], an ionic charge transfer occurs synchronously [14] or asynchronously [15] with the displacement of Cu^+ ions. In this case, the Cu^+ cations move between the two allowed positions inside the S_6 octahedra in the same P_2S_6 layer [16], until Cu^+ leaves its P_2S_6 layer and interacts with S in the frame of the S_6 octahedra of the neighboring P_2S_6 layer through the vdW gap [14]. From the theoretical standpoint, the polarization dynamics in vdW and related ferroelectric materials is governed by an effective multiwell free energy landscape of the order parameters [10–13,17]. The LGD approach [18–20] can be applied to describe the polarization reversal inside the P_2S_6 layer in CIPS [21] and related materials. LGD is less efficient in describing the contribution of interlayer polarization to the CIPS vdW gap due to their direct relationship with ionic transfer (see, e.g., Ref. [22]). However, a proper elaboration of the LGD approach made it suitable for the description of ferroionic [23,24] and antiferroionic [25,26] interactions.

Using the LGD approach here, we study strain-induced transitions of polarization reversal in thin strained CIPS films covered by ideally conductive electrodes [see Fig. 1(c)]. This paper contains the physical description of the problem (Sec. II) and analysis of the strain-induced transitions of a polarization reversal and hysteresis loop changes in the CIPS films (Sec. III). Section IV summarizes the obtained results and potential outcomes.

II. PROBLEM FORMULATION

Here, we consider an epitaxial thin CIPS film sandwiched between ideally conductive electrodes and clamped on a thick rigid substrate [see Fig. 1(c)]. Arrows show the out-of-plane ferroelectric polarization P_3 , directed along the X_3 axis. An electric voltage is applied between the electrodes.

In a general case, in-plane polarization components appear in uniaxial ferroelectric films under incomplete screening conditions (e.g., for semiconducting electrodes and/or electrically open surfaces). Namely, the flux-closure domains, which are in-plane domains, appear to decrease the depolarization field energy of the c -domain structure under incomplete screening conditions. To avoid complications related to the domain structure appearance in a uniaxial ferroelectric CIPS film, we consider the film sandwiched between two ideally conductive electrodes. The perfect electric contact between the film and ideal electrodes provides an effective screening of the out-of-plane polarization by the electrodes and prevents the formation of c domains and flux-closure domains.

Within the continuous media approximation and LGD approach, the value and orientation of the spontaneous polarization P_i in thin ferroelectric films is controlled by the temperature T and mismatch strain u_m . The strain u_m originates from the film-substrate lattice-constant mismatch and exists for the entire film depth [27–29] because the film thickness is regarded as smaller than the critical thickness of the misfit dislocation appearance. For the validity of the continuum media approximation, the film thickness is regarded as much bigger than the lattice constant. As a rule, both conditions are valid in the film thickness range 5–50 nm.

It has been shown in Refs. [11–13] that the LGD free energy density of CIPS, g_{LGD} , has four potential wells at $\vec{E} = 0$. The density g_{LGD} includes the Landau-Devonshire expansion in even powers of the polarization P_3 (up to the eighth power), the Ginzburg gradient energy, and the elastic and electrostriction energies. These are listed in Appendix A in the Supplemental Material [30]. The dynamics of polarization P_3 , piezocoefficient d_{33} , and dielectric susceptibility χ_{33} in an external field E_3 follows from the time-dependent LGD equations, which have the form:

$$\Gamma \frac{\partial P_3}{\partial t} + [\alpha - 2\sigma_i(Q_{i3} + W_{ij3}\sigma_j)]P_3 + (\beta - 4Z_{i33}\sigma_i)P_3^3 + \gamma P_3^5 + \delta P_3^7 - g_{33kl} \frac{\partial^2 P_3}{\partial x_k \partial x_l} = E_3, \quad (1a)$$

$$\Gamma \frac{\partial \chi_{33}}{\partial t} + [\alpha - 2\sigma_i(Q_{i3} + W_{ij3}\sigma_j) + 3(\beta - 4Z_{i33}\sigma_i)P_3^2 + 5\gamma P_3^4 + 7\delta P_3^6] \chi_{33} - g_{33kl} \frac{\partial^2 \chi_{33}}{\partial x_k \partial x_l} = 1, \quad (1b)$$

$$\Gamma \frac{\partial d_{33}}{\partial t} + [\alpha - 2\sigma_i(Q_{i3} + W_{ij3}\sigma_j) + 3(\beta - 4Z_{i33}\sigma_i)P_3^2 + 5\gamma P_3^4 + 7\delta P_3^6] d_{33} - g_{33kl} \frac{\partial^2 d_{33}}{\partial x_k \partial x_l} = (2Q_{33} + 2W_{i33}\sigma_i)P_3 + 4Z_{333}P_3^3. \quad (1c)$$

Here, Γ is the Khalatnikov kinetic coefficient [31]. The coefficient α depends linearly on the temperature T , $\alpha(T) = \alpha_T(T - T_C)$, where T_C is the Curie temperature of a bulk ferroelectric. The coefficients β , γ , and δ in Eqs. (1a)–(1c) are temperature independent. The values σ_i denote diagonal components of a stress tensor in the Voigt notation, and the subscripts $i, j = 1-6$. The values Q_{i3} , Z_{i33} , and W_{ij3} denote the components of a single linear and two nonlinear electrostriction strain tensors in the Voigt notation, respectively [32,33]. The values g_{33kl} are polarization gradient coefficients in the matrix notation, and the subscripts $k, l = 1-3$. Note that the contribution of nonlinear electrostriction W_{ij3} was not considered in Ref. [12]. Corresponding analytical expressions for the coefficients α^* , β^* , γ^* , and δ^* , renormalized by the mismatch strain, are derived in this paper and listed in Appendix A in the Supplemental Material [30].

The boundary condition for P_3 at the film surfaces S is natural, i.e., $g_{33kl}n_k \frac{\partial P_3}{\partial x_l} \Big|_S = 0$, where \vec{n} is the outer normal to the surface. The value E_3 in Eq. (1a) is an electric field component codirected with the polarization P_3 . In a general case, it is a superposition of external and depolarization fields. In the considered case of ideal screening, the depolarization field and domain formation are absent because ideal screening makes the solutions corresponding to constant P_3 most energetically favorable. Hence, the polarization gradient is absent in Eqs. (1a)–(1c). To analyze a quasistatic polarization reversal, we assume that the period $2\pi/\omega$ of the sinusoidal external field E_3 is very small in comparison with the Landau-Khalatnikov relaxation time $\tau = \Gamma/|\alpha|$.

The modified Hooke's law relating elastic strains u_i and stresses σ_j is obtained from the relation $u_i = -\partial g_{\text{LGD}}/\partial \sigma_i$:

$$u_i = s_{ij}\sigma_j + Q_{i3}P_3^2 + Z_{i33}P_3^4 + W_{ij3}\sigma_j P_3^2. \quad (2)$$

For the considered CIPS film, the following relations are valid for homogeneous stress and strain components: $\sigma_3 = \sigma_4 = \sigma_5 = \sigma_6 = 0$, $u_1 = u_2 = u_m$, and $u_4 = u_5 = u_6 = 0$.

The values of T_C , α_T , β , γ , δ , Q_{i3} , W_{ij3} , and Z_{i33} have been derived in Refs. [10–13] from the fitting of temperature-dependent experimental data for the dielectric permittivity [34,35], spontaneous polarization [36], and lattice constants [37] as a function of hydrostatic pressure. Elastic compliances s_{ij} were calculated from ultrasound velocity measurements [38,39]. The CIPS parameters used in our calculations are listed in Table SI in Appendix A in the Supplemental Material [30].

III. RESULTS AND DISCUSSION

A. Quasistatic behavior of polarization reversal

The strain effect on the polarization reversal in normal ferroelectric films with $Q_{33} > 0$, $Q_{23} < 0$, and $Q_{13} < 0$ typically leads to a strong increase of the out-of-plane spontaneous polarization and coercive field for tensile strains

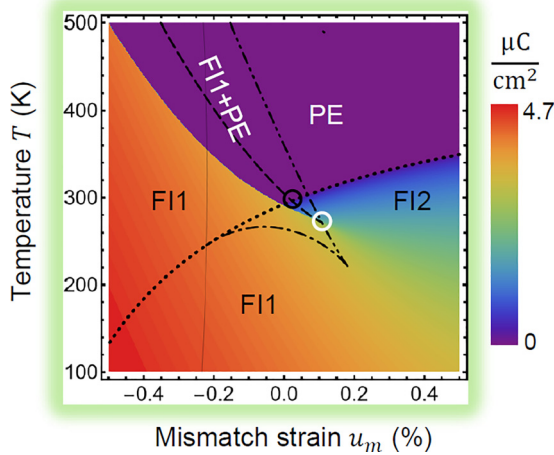


FIG. 2. The dependence of the spontaneous polarization P_s on temperature T and mismatch strain u_m . PE is the paraelectric phase, FI1 and FI2 are the ferrielectric states. CEP and BEP are the critical and bicritical endpoints, marked by the black and white circles, respectively. Color scale is the absolute value of P_s in the deepest potential well of the Landau-Ginzburg-Devonshire (LGD) free energy. CIPS parameters are listed in Table SI in the Supplemental Material [30].

and their strong decrease or disappearance for compressive strains (see, e.g., Ref. [27,29]). Due to the inverted signs of the linear electrostriction coupling coefficients ($Q_{33} < 0$, $Q_{23} > 0$, and $Q_{13} > 0$) as well as the strongly negative and temperature-dependent nonlinear electrostriction coupling coefficients ($Z_{i33} < 0$ and $W_{ij3} < 0$) for CIPS (see Table SI in the Supplemental Material [30]), we expect that the strain effect on the remanent polarization and coercive field of the CIPS film can differ in comparison with films of classical ferroelectrics. Below, we show and analyze two types of the phase diagrams: the *static* diagram (Fig. 2), which defines the thermodynamically stable polarization ground state, and the *dynamic* diagrams (Fig. 3) representing the quasistatic polarization dynamics.

The dependence of the spontaneous polarization P_s on temperature T and mismatch strain u_m is shown in Fig. 2. The diagram, which is consistent with a central part of the diagram 4(b) in Ref. [12], was calculated by a conventional numerical minimization of the free energy, Eq. (S.1) listed in Appendix A in the Supplemental Material [30]. The color scale in the diagram shows the absolute value of P_s in the deepest potential well of the LGD free energy. Here, a wedge-like region of the PE phase, which is stable at $T > 300$ K, meets the two ferrielectric states FI1 and FI2, which correspond to big and small amplitudes of the out-of-plane spontaneous polarizations P_3^\pm , respectively. The schematics of a potential relief in the PE phase and FI1 and FI2 states are shown in Fig. 1(b).

The PE-FI2 boundary is a second-order phase transition at tensile strains $u_m > 0$, and the PE-FI1 boundary is a first-order transition at compressive strains $u_m < 0$. The first-order transition stipulates the coexistence of the FI1 state and the PE phase for tensile strains, marked as the FI1+PE region. The critical endpoint (CEP), where the second-order PE-FI2 phase transition line terminates, is shown by a black circle, and the

bicritical endpoint (BEP), where the first-order isostructural phase transition line between two ferrielectric states (FI1 and FI2) with different amplitudes of spontaneous polarization terminates, is shown by a white circle. The FI1 and FI2 states merge in the BEP, creating flattening of the free energy landscape around nonzero polarization [see the dashed curve in Fig. 1(b)].

The anomalous feature of the diagram is that the high-polarization FI1 state exists at compressive strains $u_m < 0$. The state does not vanish for a tensile strain $u_m > 0$; instead, it continuously transforms in the small-polarization FI2 state at $u_m > 0$ and eventually undergoes a second-order phase transition to the PE phase at the dotted line. The situation, shown in Fig. 2 for $u_m > 0$, is anomalous for most uniaxial and multiaxial ferroelectric films, where the out-of-plane polarization is absent or very small at $u_m > 0$, and the region of the FE c phase vanishes or significantly constricts for $u_m > 0$ [27]. This analysis also illustrates that the strain effects in CIPS and similar materials can result in flattening of the free energy profile around nonzero polarization values, unlike classical ferroelectrics. Therefore, these regions can be prone to emergence of giant electromechanical and dielectric responses, as will be explored below.

The diagram in Fig. 3(a) illustrates the influence of temperature T and mismatch strain u_m on the shape of static curves and quasistatic hysteresis loops $P_3(E)$. Figure 3(b) is a zoomed central region of Fig. 3(a). The diagrams were calculated from the dynamic Eqs. (1a)–(1c) at $\omega = 0$ (for the static curves) and $\omega\tau \ll 10^{-4}$ (for quasistatic hysteresis loops). The diagrams contain a red region of PE curves (PCs); an orange region of double loops (DLs); yellow and olive regions of triple loops of the first (TL-I) and second (TL-II) types; light green, brown, and dark green regions of pinched loops of the first (PL-I), second (PL-II), and third (PL-III) types; and cyan, dark cyan, and blue regions of single loops of the first (SL-I), second (SL-II), and third (SL-III) types. The classification considers the shape of the quasistatic loops and the structure of the static curves, which are shown in Fig. 3(c) by red solid curves and thin black dashes, respectively. Note that the 10 types of static curves and quasistatic loops distinguished in thin strained CIPS films and shown in Fig. 3(c) are bigger than the eight types of static curves distinguished in CIPS nanoparticles in Ref. [13]. Equations describing different curves, which separate different regions in Fig. 3, are listed in Appendix B in the Supplemental Material [30].

The yellow and olive regions of TL-I and TL-II shown in Fig. 3(b) are located inside the blue region of the FI2 phase shown in Fig. 2. Tls fill the region inside the dotted, dashed, and dot-dot-dashed curves. The CEP and BEP are two vertices of the triangle. The region of PL-I is located above the dashed curve in the PE and FI1 coexisting region. Thin PL-II and PL-III regions are stable near the diffuse boundary between the FI2 and FI1 states. As follows from the structure of the static curves in Fig. 3(c), Tls and PLs can be imagined as the result of superposition of a central SL (corresponding to the switching of the small polarization in the FI2 state) and a DL (corresponding to the switching of a larger polarization in the FI2 state). The coexistence of these two polarizations in the four-well FI2 state determines the stability of the Tls shown in Fig. 3.

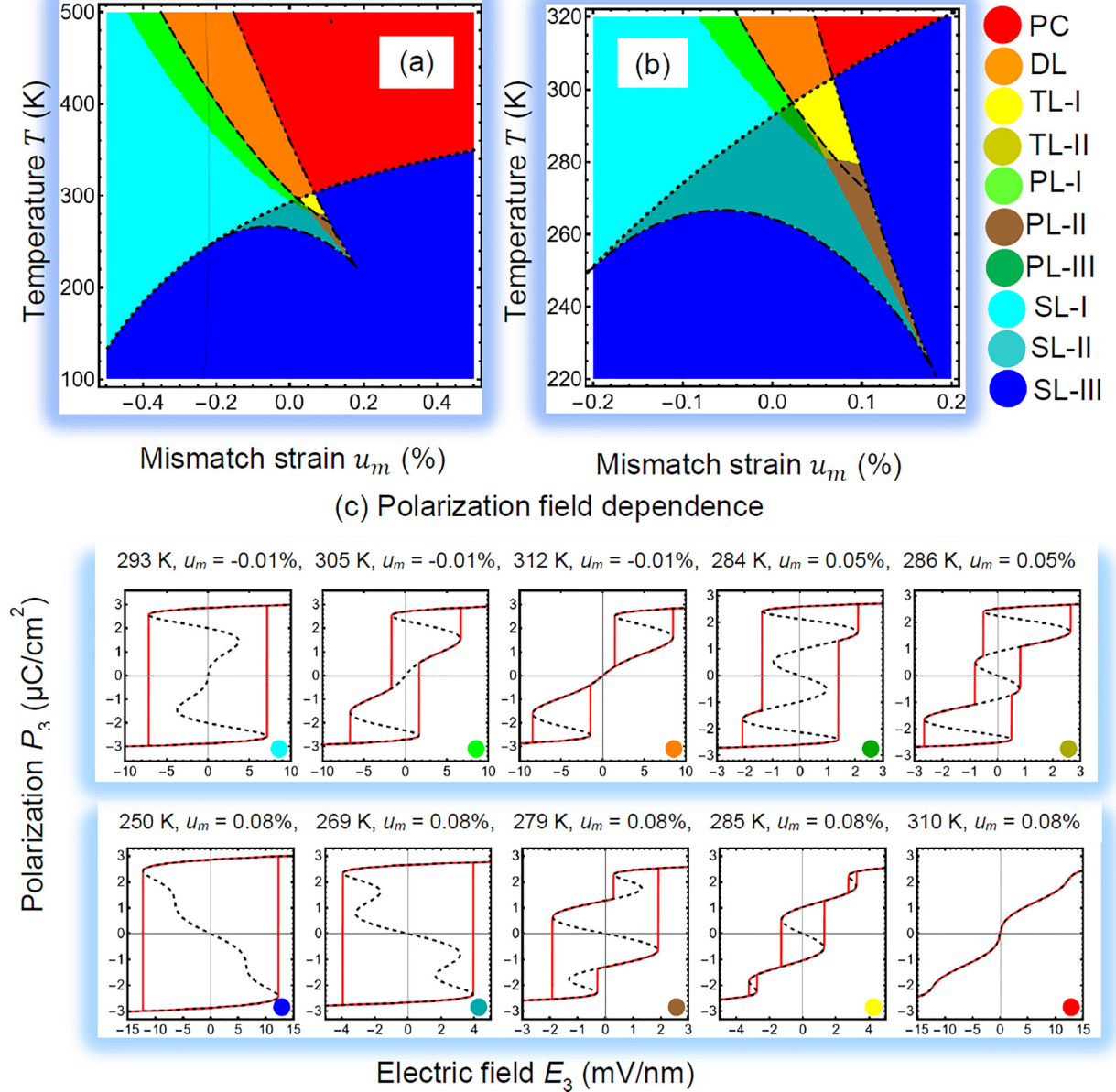


FIG. 3. (a) The shape of quasistatic hysteresis loops $P_3(E)$, calculated as a function of temperature T and mismatch strain u_m . (b) A zoomed central region of the diagram (a). Color coding in diagrams (a) and (b): red is paraelectric curve (PC); orange is double loop (DL); yellow and olive are triple loops of the first (TL-I) and second (TL-II) types; light green, brown, and dark green are pinched loops of the first (PL-I), second (PL-II), and third (PL-III) types; cyan, dark cyan, and blue are single loops of the first (SL-I), second (SL-II), and third (SL-III) types. (c) Electric field dependence of the polarization P_3 , calculated for CIPS thin films, different temperature T , and mismatch strain u_m listed above each graph. Black dashed curves are static dependences ($\omega = 0$); red solid loops are quasistatic hysteresis loops calculated for dimensionless frequency $\omega\tau = 10^{-5}$. Colors of the circles correspond to diagrams (a) and (b). CIPS parameters are listed in Table SI in the Supplemental Material [30].

The cyan region of SL-I and dark cyan region of SL-II are separated by the dotted curves in Figs. 3(a) and 3(b). The SL-I and SL-II regions are located inside the FI1 state in Fig. 2. The SL-I region is also stable in the PE and FI1 coexistence region. Big blue regions of SL-III, shown Figs. 3(a) and 3(b), are reentrant, as located inside the regions of FI1 and FI2 states absolute stability in Fig. 2. The absolute stability of the SL-III appears when the four-well potential transforms into a two-well potential.

The regions of PC and DL, separated by a dot-dot-dashed curve in Fig. 3(b), are located inside the PE phase region shown in Fig. 2. The DLs are related to the first-order phase transition induced by the electric field.

As anticipated, far from all features of the static curves are present on the quasistatic loops [compare red solid loops and black dashed curves in Fig. 3(c)]. Unstable parts of the static curves, which correspond to the negative susceptibility in Fig. 4(a), as well as those stable parts of the static curves,

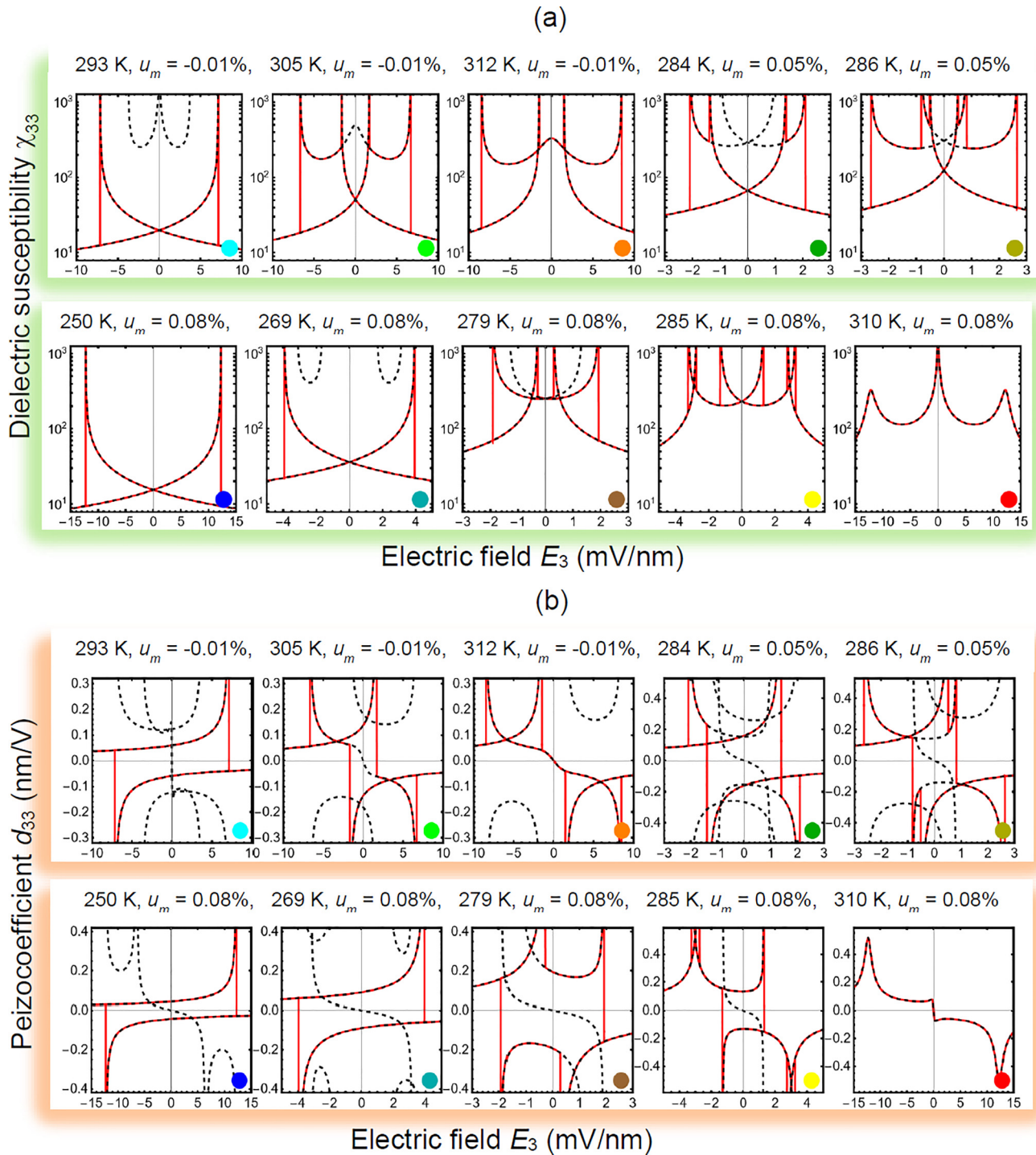


FIG. 4. Electric field dependence of (a) the dielectric susceptibility χ_{33} and (b) piezoelectric coefficient d_{33} calculated for CIPS thin films, different temperature T , and mismatch strain u_m listed above each graph. Black dashed curves are static dependences ($\omega = 0$); red solid loops are quasistatic hysteresis loops calculated for dimensionless frequency $\omega\tau = 10^{-5}$. Colors of the circles correspond to the diagrams in Figs. 3(a) and 3(b). CIPS parameters are listed in Table SI in the Supplemental Material [30].

which are located inside the SL, are never observed at the quasistatic loops. At the same time, static curves and quasistatic loops of dielectric susceptibility χ_{33} and piezoelectric coefficient d_{33} , shown in Figs. 4(a) and 4(b), reflect all features of the polarization static curves and quasistatic loops, respectively. The static curves of χ_{33} and d_{33} have divergencies at coercive fields and/or sharp jumps, their position coinciding

with the jumps on polarization static curves. The quasistatic loops of χ_{33} and d_{33} almost coincide with the static curves, except for the unstable parts and divergencies at coercive fields. The divergencies transform into sharp maxima, their height decreasing with increase in frequency ω . The quasistatic loops of χ_{33} and d_{33} contain two, four, or six features (jumps and/or sharp maxima), which correspond to different

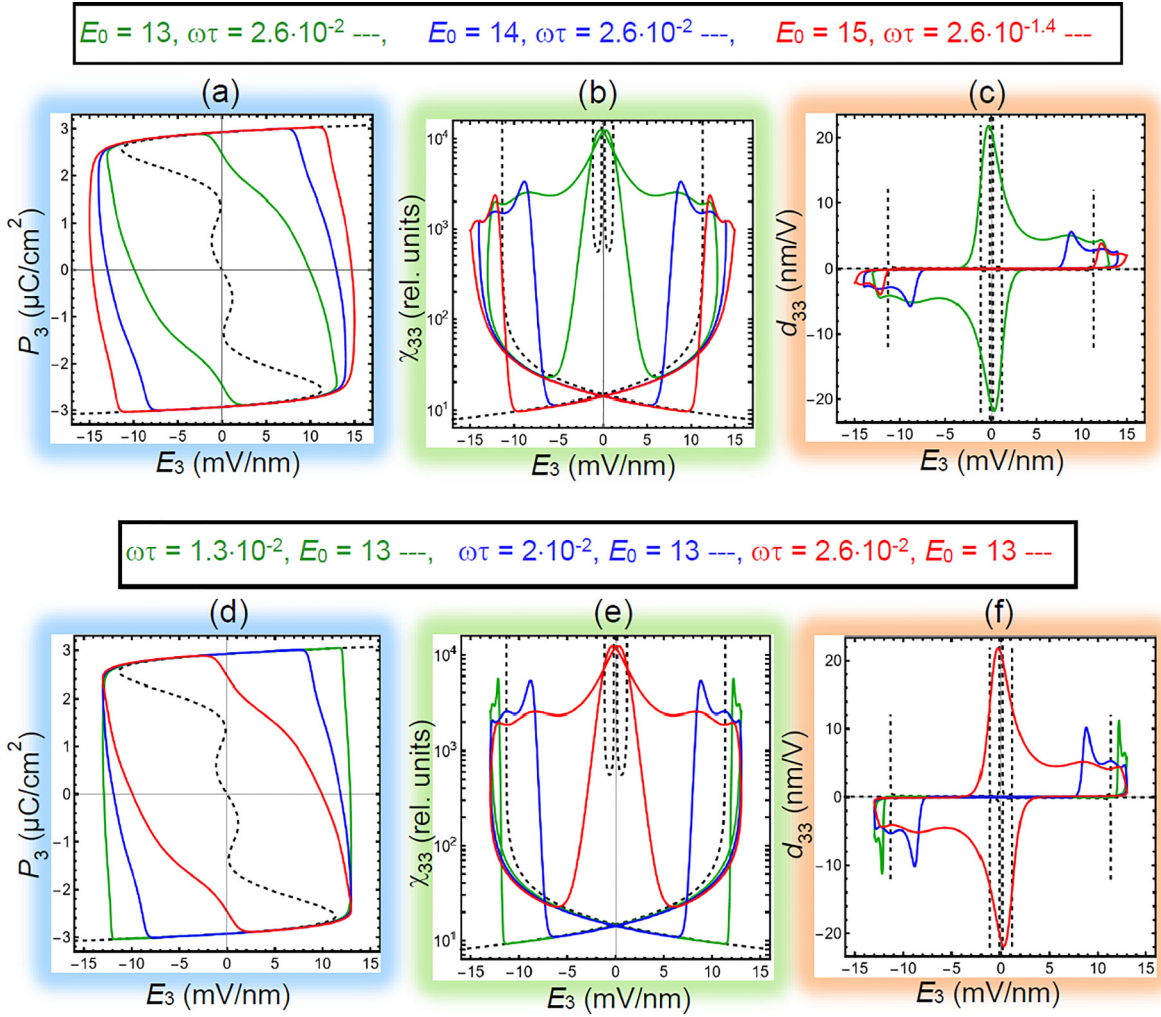


FIG. 5. Electric field dependence of (a) and (d) the polarization P_3 , (b) and (e) dielectric susceptibility χ_{33} , and (c) and (f) piezoelectric coefficient d_{33} calculated for CIPS thin films. Black dashed curves are static dependences ($\omega = 0$). Green, blue, and red solid curves are dynamic hysteresis loops calculated for (a)–(c) different amplitudes $E_0 = (13\text{--}15)$ mV/nm of applied field and the same frequency $\omega\tau = 2.6 \times 10^{-2}$ or (d)–(f) for different frequencies $\omega\tau = (1.3\text{--}2.6) \times 10^{-2}$ of applied field and the same amplitude $E_0 = 13$ mV/nm. CIPS parameters are listed in Table SI in the Supplemental Material [30], $T = 276$ K and $u_m = 0.01\%$.

types of SLs, PLs, or TLs, respectively. Some of these features are hardly seen on the polarization loops, especially under the transition from one type of loop to another. However, the features are much better seen on the loops of susceptibility and piezoelectric, and thus, the simultaneous measurements of the polarization, susceptibility, and piezoelectric response can help to verify our theoretical predictions.

An important peculiarity of Figs. 3 and 4 is the strong influence of the elastic strain on the features of quasistatic polarization reversal in thin CIPS films, namely, the variability of hysteresis loops shapes and particularly the existence of the PL and TL regions at $u_m < 0.2\%$. This is due to the specific structure of the static curves, which is determined by the eighth-order LGD potential. The absence of PC and DL at compressive strains $u_m < 0$ and $T < 300$ K originates from the anomalous temperature dependence and inverted sign of the CIPS linear and nonlinear electrostriction coupling coefficients (see Table S1 in the Supplemental Material [30]).

B. Low-frequency behavior of polarization reversal

The low-frequency hysteresis loops of polarization P_3 , piezoelectric coefficient d_{33} , and relative dielectric susceptibility χ_{33} , calculated for frequencies $\omega\tau \leq 10^{-3}$, look very similar to the quasistatic loops shown in Figs. 3(c) and 4. However, polarization hysteresis loops calculated in the frequency range $10^{-2} \leq \omega\tau \leq 5 \times 10^{-1}$ may have a negative slope in a relatively narrow range of external field amplitude E_0 and definite ranges of temperature and mismatch strain [see e.g., red, blue and green loops in Figs. 5(a) and 5(d)]. The negative slope can be observed for those hysteresis loops whose static curves have three unstable regions and two touch points with the P axis [see e.g., black dashed curves in Figs. 5(a) and 5(d)].

One should expect that the negative slope of hysteresis loops may correspond to the negative relative dielectric susceptibility, which is transient in the considered case ($\omega\tau > 10^{-2}$). Indeed, the metastable parts of dashed black curves in

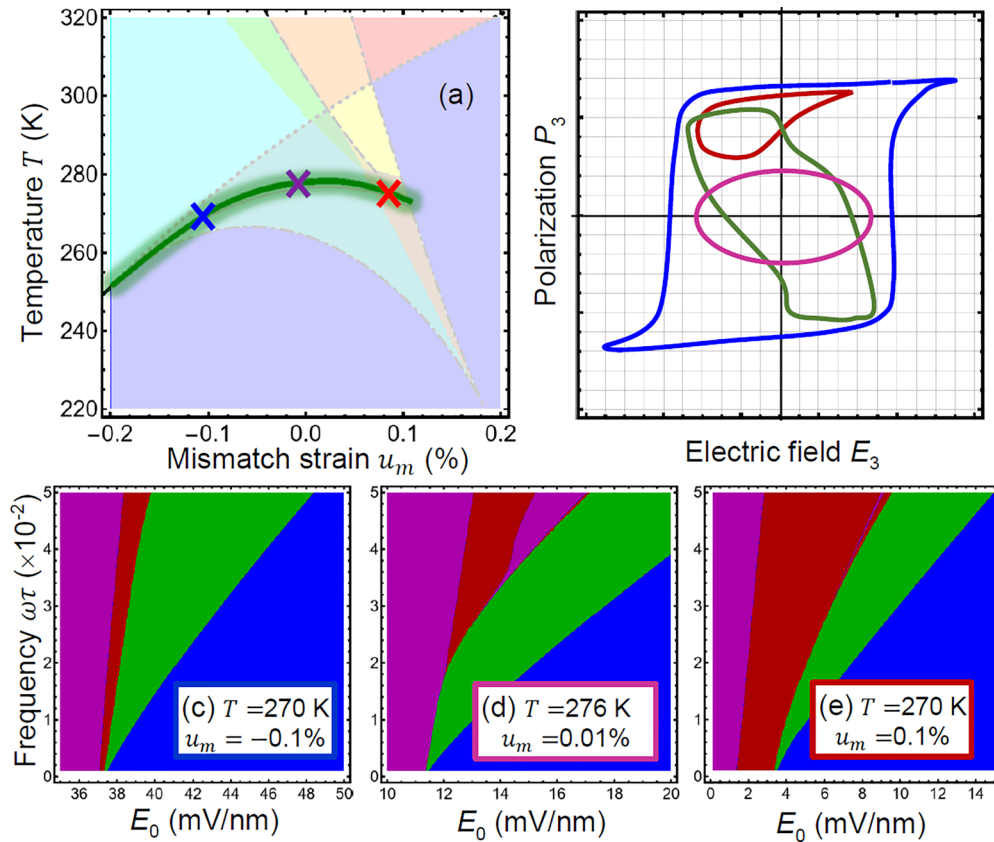


FIG. 6. (a) The ranges of temperature T and mismatch strain u_m for which the negative slope of polarization hysteresis loops can be observed in definite intervals of dimensionless frequency $\omega\tau$ and external field amplitude E_0 , shown by the diffuse dark green curve. (b) The schematic image of the polarization partial switching (dark red), the elliptic loop of polarization (dark magenta), the polarization hysteresis loop with a negative slope (dark green), and the polarization hysteresis loop with a positive slope (blue). (c)–(e) The ranges of $\omega\tau$ and E_0 for which the polarization partial switching (dark red region), elliptic loop hysteresis loops with a negative slope (dark green region), elliptic and quasicircular loops (dark magenta region), and hysteresis loops with a positive slope (blue region) are observed. Diagrams (c)–(e) are calculated for different T and u_m listed in the legends, which also correspond to the blue, violet, and red crosses in diagram (a). CIPS parameters are listed in Table SI in the Supplemental Material [30].

Figs. 5(a) and 5(d) correspond to negative values of static susceptibility. A point-by-point derivative dP_3/dE_3 , calculated numerically using the points of solid curves, is negative in the region of negative slope, allowing us to speculate about the possibility of transient negative capacitance of the film. However, the true dielectric susceptibility χ_{33} , calculated from Eq. (1b) for parameters, which corresponds to the solid loops in the plots in Figs. 5(a) and 5(d), is positive, as anticipated from the thermodynamic equilibrium principle. This positive susceptibility is shown in Figs. 5(b) and 5(e).

Interestingly, the susceptibility and piezoelectric coefficient hysteresis loops, shown in Figs. 5(b), 5(c) and 5(e), 5(f), which correspond to the green polarization loop with negative slope in Fig. 5(a) and red polarization loop with negative slope in Fig. 5(d), reach giant values (such as $\chi_{33} > 10^4$ and $d_{33} > 5$ nm/V) for the entire the range of field changes and are maximal for small fields. The susceptibility and piezoelectric loops, calculated for higher E_0 and shown by the blue and red loops in Figs. 5(b) and 5(c), as well as by blue and green loops in Figs. 5(d) and 5(f), are significantly smaller and reach maximal values in a relatively wide vicinity of the coercive field. In contrast with the single hysteresis loops in many uniaxial ferroelectrics described by a two- or

three-well LGD potential (corresponding to the 2–4 powers or 2–4–6 powers of polarization series, respectively), the loops of dielectric susceptibility and piezoelectric for CIPS films have additional maxima near coercive fields originating from its four-well LGD potential (corresponding to the 2–4–6–8 powers of polarization series).

The giant values χ_{33} and d_{33} , which correspond to the polarization hysteresis loops with negative slope, present further interest and can be useful for practical applications. Hence, we proceed to determine the ranges of temperature T and mismatch strain u_m for which the negative slope can be observed. Using analytical conditions listed in Appendix B in the Supplemental Material [30] and the numerical algorithm described in Appendix C in the Supplemental Material [30], we determined the intervals of dimensionless frequency $\omega\tau$ and external field amplitude E_0 for which the polarization hysteresis loops have negative slope for definite values of T and u_m . The corresponding dependence of T on u_m is shown by a thick dark green curve surrounded by a diffuse green region in Fig. 6(a). The green curve is calculated from Eqs. (S.10a) and (S.10b), which are listed in Appendix B in the Supplemental Material [30]. Equation (S.10) in the Supplemental Material [30] determines the conditions of zero coercive field for

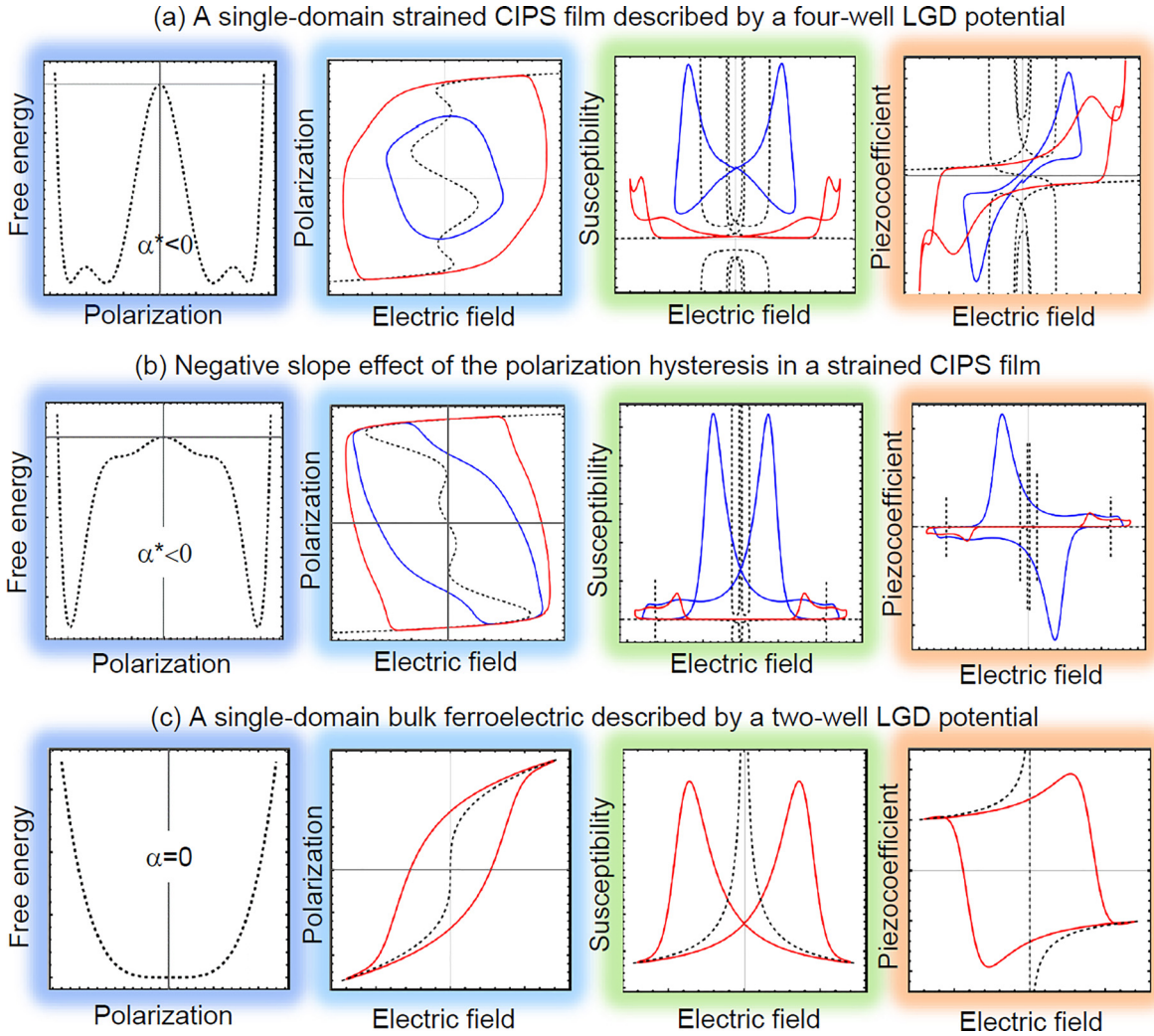


FIG. 7. A single-domain strained CIPS film described by (a) a four-well Landau-Ginzburg-Devonshire (LGD) potential, (b) negative slope effect of the polarization hysteresis in the film, and (c) a single-domain bulk ferroelectric described by a two-well LGD potential calculated for $\alpha = 0$: free energy dependence on polarization (left), polarization P_3 , dielectric susceptibility χ_{33} , and piezocoefficient d_{33} dependence on electric field E_3 (right). Black dashed curves are static dependences ($\omega = 0$). Solid curves are dynamic hysteresis loops calculated for smaller (blue) and bigger (red) amplitudes E_0 of applied field and the same frequency $\omega\tau \cong 10^{-2}$, where $\tau = \Gamma/|\alpha_T T_C|$.

internal unstable parts of the static curves shown in, e.g., Figs. 5(a) and 5(d). The diagrams in Figs. 6(c)–6(e) show the ranges of $\omega\tau$ and E_0 , for which either the partial switching of polarization, hysteresis loops with a negative slope, or hysteresis loops with a positive slope are stable for $T \cong 270$ –275 K, negative, almost zero, or positive u_m , respectively. In the diagrams, the dark green region of the loops with a negative slope separates the dark red region of a partial switching from the blue region of the loops with a positive slope. Notably, the E_0 width of the dark green region is very small for $\omega\tau < 10^{-2}$ but strongly increases with $\omega\tau$ increase $> 10^{-2}$, indicating the transient nature of the negative slope effect. For further frequency increase, loops with negative slope eventually transform into quasicircular or elliptic loops.

C. Discussion

Now one may ask, how individual are the polarization reversal features we found for thin strained CIPS films,

which are described by the four-well 2–4–6–8-power LGD potential? The most interesting anomalies of the polarization behavior are observed near phase transitions and CEPs and BEPs. In Fig. 7, the top and middle rows show the anomalies of the polarization behavior in a strained CIPS film. The bottom row illustrates the well-known behavior of a uniaxial single-domain bulk ferroelectric described by the sixth-order Landau-Devonshire potential $g_{LD} = \frac{\alpha}{2}P_3^2 + \frac{\beta}{4}P_3^4 + \frac{\gamma}{6}P_3^6$, for the case $\alpha = 0$, $\beta > 0$, and $\gamma > 0$, which corresponds to the flat well at the ferroelectric-PE transition point. We emphasize that the sixth-order Landau-Devonshire expansion cannot reveal the four-well potential relief responsible for the appearance of the FI1 and FI2 states nor the TLs and loops with negative slope. For nonzero α , the sixth-order expansion can demonstrate a single-, two-, or three-well potential relief with a central well and two side wells.

Figure 7(a) shows the case in which the polarization dependence of the CIPS free energy has four equal potential wells (the first on the left plot). Corresponding polarization,

dielectric susceptibility, and piezocoefficient dependences on the electric field are shown in the second-on-the-left and two plots on the right, respectively. Black dashed curves, which contain three unstable regions, are static dependences. Round-shaped solid loops are low-frequency polarization hysteresis loops calculated for smaller (blue) and bigger (red) amplitudes E_0 of applied field. The static dependencies of dielectric susceptibility and piezocoefficient have a complex shape with six divergencies. The low-frequency dielectric susceptibility and piezocoefficient loops have anomalous shapes with several maxima and self-crossing, which in fact are conditioned by the structure of the static dependences.

Figure 7(b) shows the case in which the dependence of CIPS film free energy on polarization has two deep potential wells and two inflection points (the first on the left plot). The corresponding polarization hysteresis with a negative slope is shown in the second-on-the-left plot for smaller (blue) and bigger (red) amplitudes E_0 . The field dependences of dielectric susceptibility and piezocoefficient are shown in the right plots. Black dashed curves, which contain three unstable regions and two touch points with the P axis, are static dependences. The static dependencies of dielectric susceptibility and piezocoefficient look like six very narrow divergent peaks. The low-frequency dielectric susceptibility and piezocoefficient loops have anomalous shapes with several maxima and self-crossing, whose positions are different from the static dependences.

Both static and low-frequency dependences, shown in Figs. 7(a) and 7(b), have principal differences from the corresponding dependences of a single-domain bulk ferroelectric described by a flat-well Landau-Devonshire potential in the vicinity of the ferroelectric-PE transition point [see Fig. 7(c)]. Hence, the above features look individual for CIPS and related ferroelectric or ferrielectric materials, whose free energy profiles can flatten in the vicinity of the nonzero polarization states.

The next question is, which of these features will survive in the epitaxial CIPS films covered with nonideal electrodes or surface screening charges? The answer depends on the so-called effective screening length λ of the nonideal electrodes, which should be small enough to prevent the domain formation in the film. Our calculations for CIPS, as well as earlier LGD-based calculations for classical first- and second-order ferroelectric materials [40], show that, as a rule, the single-domain state remains stable for $\lambda \leq 0.01$ nm in a 20–50-nm-thick film. The value 0.02 nm corresponds to a semimetallic electrode, such as SrRuO₃ with carrier concentration $\sim 10^{28}$ m⁻³, and the λ values < 0.01 nm are reached in metallic (e.g., Pt, Ag, or Au) electrodes. Thus, to verify the effects predicted in this paper, one rather needs to provide an ideal electric contact between the epitaxial film and the standard metallic electrodes.

Noteworthy, in this paper, we consider the intralayer polarization states in CIPS films, for which spontaneous polarization does not exceed $5 \mu\text{C}/\text{cm}^2$, and the polarization is reversed by a relatively small homogeneous electric field applied between the ideally conducting electrodes. The hysteresis loops, shown in Figs. 3(c), 4, and 5, correspond to relatively small misfit strains ($< 0.5\%$), when Cu atoms remain within their layers and do not travel in the vdW gap. Direct

experimental evidence for these loops is absent because available measurements of local polarization reversal by, e.g., piezoelectric force microscope tip [14], are, as a rule, accompanied by the nanodomain formation, which cardinally changes the loop shape (see, e.g., Fig. 2 in Ref. [13]). In the case of macroscopic polarization reversal in capacitor geometry, lattice barriers and pinning effects, which are not considered in this paper, can lead to significant smearing of the piezoelectric response and dielectric susceptibility hysteresis loops. Indirect evidence of anomalous negative nonlinear electrostriction coupling, which is the key feature of our LGD model, can be found in recent Refs. [41,42]. However, in both cases, high stresses, either indentation or pressure, increase the CIPS polarization $> 5 \mu\text{C}/\text{cm}^2$ and move Cu atoms into the interlayer positions. A combination of the first-principles and modified LGD approaches may quantitatively describe the recent experimental results.

IV. CONCLUSIONS

Using the eighth-order LGD free energy expansion in polarization powers, we study strain-induced transitions of polarization reversal scenarios in CIPS thin films covered by ideally conductive electrodes. Due to multiple potential wells, whose height and position are temperature and strain dependent, the energy profiles of CIPS can flatten in the vicinity of nonzero polarization states. Thus, CIPS differs from classical ferroelectric materials with first- or second-order ferroelectric-PE phase transitions, whose potential energy profiles can be shallow or flat near the transition points only, corresponding to zero spontaneous polarization. Due to the difference, we reveal an unusually strong influence of a mismatch strain on the out-of-plane polarization reversal, hysteresis loop shape, dielectric susceptibility, and piezoelectric response of the strained CIPS films. By varying the sign of the mismatch strain (from tension to compression) and its magnitude (from 0 to 0.2%), quasistatic hysteresisless PCs can transform into double, triple, and different types of pinched and single hysteresis loops. The specific shape of the quasistatic hysteresis loops is defined by static dependences of polarization on an applied electric field, referred to as static curves, which can contain one, two, or four unstable parts, related to a multiwell LGD potential of CIPS.

The predicted strain effect on the polarization reversal is opposite, i.e., anomalous, in comparison with many other ferroelectric films: The out-of-plane remanent polarization enhances strongly, and coercive field increases for tensile strains; meanwhile, the polarization decreases strongly or even disappears, and hysteresis characteristics worsen significantly for compressive strains. We explain this effect by inverted signs of linear and nonlinear electrostriction coupling coefficients of CIPS and their strong temperature dependence.

For definite values of temperature and mismatch strain, the low-frequency hysteresis loops of polarization may have a negative slope in the relatively narrow range of external field amplitude and frequency. The negative slope of hysteresis loops can be observed in the states with a four-well LGD potential, which has two deep wells and either two very shallow wells or two inflection points. The field width of the negative slope region strongly increases with the frequency

increase. For further frequency increase, loops with negative slope eventually transform into quasicircular or elliptic loops, indicating the transient nature of the negative slope effect, and eventually transform into quasicircular or elliptic loops. Notably, the low-frequency susceptibility hysteresis loops, which correspond to the negative slope of polarization loops, contain only positive values, which can be giant (such as 10^4) in the entire range of field changes and are maximal at very small fields. The corresponding piezoelectric response can also reach giant values (>5 nm/V) in the entire range of field changes being maximal near coercive fields.

Numerical results presented in this paper are obtained and visualized using specialized software, Mathematica 13.1 [43]. The Mathematica notebook, which contain the codes, is available per reasonable request.

ACKNOWLEDGMENTS

S.V.K. was supported by the center for 3D Ferroelectric Microelectronics (3DFeM), an Energy Frontier

Research Center funded by the U.S. Department of Energy (DOE), Office of Science, Basic Energy Sciences under Award No. DE-SC0021118. A.N.M. acknowledges support from the National Research Fund of Ukraine (Project “Low-dimensional graphene-like transition metal dichalcogenides with controllable polar and electronic properties for advanced nanoelectronics and biomedical applications,” Grant Application No. 2020.02/0027). E.A.E. acknowledges support from the National Academy of Sciences of Ukraine. Authors are very grateful to Prof. Nicholas Morozovsky (NASU) for useful discussions and valuable suggestions.

The research idea belongs to A.N.M., Yu.M.V., and S.V.K. A.N.M. formulated the problem, performed analytical calculations, analyzed results, and wrote the manuscript draft. E.A.E. and M.E.Y. wrote codes and prepared the Supplemental Material. A.G. provided atomic structure models. Yu.M.V. and S.V.K. worked on the results explanation and manuscript improvement. All coauthors discussed the obtained results.

-
- [1] J. Z. Zhao, L. C. Chen, B. Xu, B. B. Zheng, J. Fan, and H. Xu, Strain-tunable out-of-plane polarization in two-dimensional materials, *Phys. Rev. B* **101**, 121407 (2020).
- [2] Z.-Z. Sun, W. Xun, L. Jiang, J.-L. Zhong, and Y.-Z. Wu, Strain engineering to facilitate the occurrence of 2D ferroelectricity in CuInP_2S_6 monolayer, *J. Phys. D: Appl. Phys.* **52**, 465302 (2019).
- [3] Ju. Banys, A. Dziaugys, K. E. Glukhov, A. N. Morozovska, N. V. Morozovsky, and Yu. M. Vysochanskii, *Van der Waals Ferroelectrics: Properties and Device Applications of Phosphorous Chalcogenides* (John Wiley & Sons, Weinheim, 2022), pp 400.
- [4] Y. M. Vysochanskii, V. A. Stephanovich, A. A. Molnar, V. B. Cajipe, and X. Bourdon, Raman spectroscopy study of the ferrielectric-paraelectric transition in layered CuInP_2S_6 , *Phys. Rev. B* **58**, 9119 (1998).
- [5] N. Sivasdas, P. Doak, and P. Ganesh, Anharmonic stabilization of ferrielectricity in CuInP_2S_6 , *Phys. Rev. Res.* **4**, 013094 (2022).
- [6] J. A. Brehm, S. M. Neumayer, L. Tao, A. O’Hara, M. Chyashnavichus, M. A. Susner, M. A. McGuire, S. V. Kalinin, S. Jesse, P. Ganesh *et al.*, Tunable quadruple-well ferroelectric van der Waals crystals, *Nat. Mater.* **19**, 43 (2020).
- [7] X. Bourdon, V. Maisonneuve, V. B. Cajipe, C. Payen, and J. E. Fischer, Copper sublattice ordering in layered CuMP_2Se_6 ($M = \text{In, Cr}$), *J. All. Comp.* **283**, 122 (1999).
- [8] V. Maisonneuve, V. B. Cajipe, A. Simon, R. Von Der Muhll, and J. Ravez, Ferrielectric ordering in lamellar CuInP_2S_6 , *Phys. Rev. B* **56**, 10860 (1997).
- [9] W. Selke and J. Oitmaa, Monte Carlo study of mixed-spin $S = (\frac{1}{2}, 1)$ Ising ferrimagnets, *J. Phys.: Condensed Matter* **22**, 076004 (2010).
- [10] A. N. Morozovska, E. A. Eliseev, K. Kelley, Yu. M. Vysochanskii, S. V. Kalinin, and P. Maksymovych, Phenomenological description of bright domain walls in ferroelectric-antiferroelectric layered chalcogenides, *Phys. Rev. B* **102**, 174108 (2020).
- [11] A. N. Morozovska, E. A. Eliseev, Yu. M. Vysochanskii, V. V. Khist, and D. R. Evans, Screening-induced phase transitions in core-shell ferroic nanoparticles, *Phys. Rev. Mater.* **6**, 124411 (2022).
- [12] A. N. Morozovska, E. A. Eliseev, S. V. Kalinin, Y. M. Vysochanskii, and Petro Maksymovych, Stress-induced phase transitions in nanoscale CuInP_2S_6 , *Phys. Rev. B* **104**, 054102 (2021).
- [13] A. N. Morozovska, E. A. Eliseev, M. E. Yelisieiev, Yu. M. Vysochanskii, and D. R. Evans, Stress-Induced Transformations of Polarization Switching in CuInP_2S_6 Nanoparticles, *Phys. Rev. Appl.* **19**, 054083 (2023).
- [14] S. M. Neumayer, L. Tao, A. O’Hara, J. Brehm, M. Si, P. Y. Liao, T. Feng, S. V. Kalinin, P. D. Ye, S. T. Pantelides *et al.*, Alignment of Polarization Against an Electric Field in van der Waals Ferroelectrics, *Phys. Rev. Appl.* **13**, 064063 (2020).
- [15] A. O’Hara, Nina Balke, and S. T. Pantelides, Unique features of polarization in ferroelectric ionic conductors, *Adv. Electron. Mater.* **8**, 2100810 (2022).
- [16] D. Zhang, Z.-D. Luo, Y. Yao, P. Schoenherr, C. Sha, Y. Pan, P. Sharma, M. Alexe, and J. Seidel, Anisotropic ion migration and electronic conduction in van der Waals ferroelectric CuInP_2S_6 , *Nano Lett.* **21**, 995 (2021).
- [17] S. M. Neumayer, N. Bauer, S. Basun, B. S. Conner, M. A. Susner, M. O. Lavrentovich, and P. Maksymovych, Dynamic stabilization of metastable states in triple-well ferroelectric $\text{Sn}_2\text{P}_2\text{S}_6$, *Adv. Mater.* **35**, 2211194 (2023).
- [18] A. Belianinov, Q. He, A. Dziaugys, P. Maksymovych, E. Eliseev, A. Borisevich, A. Morozovska, J. Banys, Y. Vysochanskii, and S. V. Kalinin, CuInP_2S_6 room temperature layered ferroelectric, *Nano Lett.* **15**, 3808 (2015).
- [19] M. Chyashnavichyus, M. A. Susner, A. V. Ievlev, E. A. Eliseev, S. V. Kalinin, N. Balke, A. N. Morozovska, M. A. McGuire, and P. Maksymovych, Size-effect in layered ferrielectric CuInP_2S_6 , *Appl. Phys. Lett.* **109**, 172901 (2016).

- [20] S. M. Neumayer, E. A. Eliseev, M. A. Susner, A. Tselev, B. J. Rodriguez, J. A. Brehm, S. T. Pantelides, G. Panchapakesan, S. Jesse, S. V. Kalinin *et al.*, Giant negative electrostriction and dielectric tunability in a van der Waals layered ferroelectric, *Phys. Rev. Mater.* **3**, 024401 (2019).
- [21] S. Zhou, L. You, A. Chaturvedi, S. A. Morris, J. S. Herrin, N. Zhang, A. Abdelsamie, Y. Hu, J. Chen, Y. Zhou *et al.*, Anomalous polarization switching and permanent retention in a ferroelectric ionic conductor, *Mater. Horiz.* **7**, 263 (2020).
- [22] S. Zhou, Lu You, H. Zhou, Y. Pu, Z. Gui, and J. Wang, Van der Waals layered ferroelectric CuInP_2S_6 : Physical properties and device applications, *Front. Phys.* **16**, 13301 (2021).
- [23] S. M. Yang, A. N. Morozovska, R. Kumar, E. A. Eliseev, Y. Cao, L. Mazet, N. Balke, S. Jesse, R. Vasudevan, C. Dubourdieu *et al.*, Mixed electrochemical-ferroelectric states in nanoscale ferroelectrics, *Nat. Phys.* **13**, 812 (2017).
- [24] A. N. Morozovska, E. A. Eliseev, N. V. Morozovsky, and S. V. Kalinin, Ferroionic states in ferroelectric thin films, *Phys. Rev. B* **95**, 195413 (2017).
- [25] A. N. Morozovska, E. A. Eliseev, A. I. Kurchak, N. V. Morozovsky, R. K. Vasudevan, M. V. Strikha, and S. V. Kalinin, Effect of surface ionic screening on polarization reversal scenario in ferroelectric thin films: Crossover from ferroionic to antiferroionic states, *Phys. Rev. B* **96**, 245405 (2017).
- [26] A. N. Morozovska, E. A. Eliseev, A. Biswas, N. V. Morozovsky, and S. V. Kalinin, Effect of Surface Ionic Screening on Polarization Reversal and Phase Diagrams in Thin Antiferroelectric Films for Information and Energy Storage, *Phys. Rev. Appl.* **16**, 044053 (2021).
- [27] N. A. Pertsev, A. G. Zembilgotov, and A. K. Tagantsev, Effect of Mechanical Boundary Conditions on Phase Diagrams of Epitaxial Ferroelectric Thin Films, *Phys. Rev. Lett.* **80**, 1988 (1998).
- [28] C. Ederer and N. A. Spaldin, Effect of Epitaxial Strain on the Spontaneous Polarization of Thin Film Ferroelectrics, *Phys. Rev. Lett.* **95**, 257601 (2005).
- [29] A. Kvasov and A. K. Tagantsev, Role of high-order electromechanical coupling terms in thermodynamics of ferroelectric thin films, *Phys. Rev. B* **87**, 184101 (2013).
- [30] See Supplemental Material at <http://link.aps.org/supplemental/10.1103/PhysRevB.108.054107> for a mathematical formulation of the problem, a table of material parameters, a description of methods, and numerical algorithms.
- [31] L. D. Landau and I. M. Khalatnikov, On the anomalous absorption of sound near a second order phase transition point, *Dokl. Akad. Nauk SSSR* **96**, 496 (1954).
- [32] Yu. M. Vysochanskii, M. M. Mayor, V. M. Rizak, V. Yu. Slivka, and M. M. Khoma, The tricritical Lifshitz point on the phase diagram of $\text{Sn}_2\text{P}_2(\text{Se}_x\text{S}_{1-x})_6$, *Zh. Eksp. Teor. Fiz.* **95**, 1355 (1989) [*Sov. Phys. JETP* **68**, 782 (1989)].
- [33] A. Kohutych, R. Yevych, S. Perechinskii, V. Samulionis, J. Banys, and Yu. Vysochanskii, Sound behavior near the Lifshitz point in proper ferroelectrics, *Phys. Rev. B* **82**, 054101 (2010).
- [34] P. Guranich, V. Shusta, E. Gerzanich, A. Slivka, I. Kuritsa, and O. Gomonnai, Influence of hydrostatic pressure on the dielectric properties of CuInP_2S_6 and $\text{CuInP}_2\text{Se}_6$ layered crystals, *J. Phys.: Conf. Ser.* **79**, 012009 (2007).
- [35] A. V. Shusta, A. G. Slivka, V. M. Kedylich, P. P. Guranich, V. S. Shusta, E. I. Gerzanich, and I. P. Prits, Effect of uniaxial pressure on dielectric properties of CuInP_2S_6 crystals, *Sci. Bull. Uzhhorod Univ. Phys.* **28**, 44 (2010).
- [36] A. Kohutych, V. Liubachko, V. Hryts, Yu. Shiposh, M. Kundria, M. Medulych, K. Glukhov, R. Yevych, and Yu. Vysochanskii, Phonon spectra and phase transitions in van der Waals ferroics $\text{MM}'\text{P}_2\text{X}_6$, *Mol. Cryst. Liq. Cryst.* **747**, 14 (2022).
- [37] M. A. Susner, M. Chyasnavichyus, A. A. Poretzky, Q. He, B. S. Conner, Y. Ren, D. A. Cullen, P. Ganesh, D. Shin, H. Demir *et al.*, Cation-eutectic transition via sublattice melting in $\text{CuInP}_2\text{S}_6/\text{In}_{4/3}\text{P}_2\text{S}_6$ van der Waals layered crystals, *ACS nano* **11**, 7060 (2017).
- [38] J. Banys, J. Macutkevicius, V. Samulionis, A. Brilingas, and Yu. Vysochanskii, Dielectric and ultrasonic investigation of phase transition in CuInP_2S_6 crystals, *Ph. Transit.* **77**, 345 (2004).
- [39] V. Samulionis, J. Banys, Yu. Vysochanskii, and V. Cajipe, Elastic and electromechanical properties of new ferroelectric-semiconductor materials of $\text{Sn}_2\text{P}_2\text{S}_6$ family, *Ferroelectrics* **257**, 113 (2001).
- [40] I. S. Vorotiahin, E. A. Eliseev, Q. Li, S. V. Kalinin, Yu. A. Genenko, and A. N. Morozovska, Tuning the polar states of ferroelectric films via surface charges and flexoelectricity, *Acta Mater.* **137**, 85 (2017).
- [41] W. Yang, S. Chen, X. Ding, J. Sun, and J. Deng, Reducing threshold of ferroelectric domain switching in ultrathin two-dimensional CuInP_2S_6 ferroelectrics via electrical-mechanical coupling, *J. Phys. Chem. Lett.* **14**, 379 (2023).
- [42] X. Yao, Y. Bai, C. Jin, X. Zhang, Q. Zheng, Z. Xu, L. Chen, S. Wang, Y. Liu, J. Wang *et al.*, Anomalous polarization enhancement in a vdW ferroelectric material under pressure, *Nat. Commun.* **14**, 4301 (2023).
- [43] <https://www.wolfram.com/mathematica>.